GEOMETRY-ALIGNED MOVING FRAMES BY REMOVING SPURIOUS DIVERGENCE IN CURVILINEAR MESH WITH GEOMETRIC APPROXIMATION ERROR

A PREPRINT

Sehun Chun, *

Underwood International College, Yonsei University, South Korea, sehun.chun@yonsei.ac.kr

February 28, 2025

ABSTRACT

The vertices of curvilinear elements usually lie on the exact domain. However, the additional grid points introduced for the higher-order polynomial of numerical solution often are located slightly out of the domain to generate geometric approximation error. Considered the main cause of the conservational error, this error is relatively smaller than discretization error but large enough to significantly deteriorate a long time integration. This paper proposes a novel scheme with geometry-aligned moving frames and the removal of corresponding spurious divergence to reduce the conservational error caused by geometric approximation error.

1 Introduction

A curvilinear mesh has been widely welcomed by various computational communities because it supports a larger element, particularly in a highly-curved region. Consequently, it provides a larger time marching step and better approximation of the domain. Thus, the curvilinear mesh shows better accuracy and efficiency. However, one critical problem with curvilinear mesh is the additional grid points beyond the triangular or quadrilateral elements' vertices. Then are introduced when the order of polynomial for the numerical solution is higher than one. However, the location of these points does not always lie exactly on the domain to cause geometric approximation error. Increasing the polynomial order (p) does not reduce this error, and only decreasing the edge length (h) of every element would do.

Several efforts have been made to remove the geometric approximation error in curvilinear meshes. One of them is a high-order mesh generator NekMesh by relocating the additional grid points such that they also stay on the curved domain with the optimal accuracy of integration [8, 9, 13, 14]. The location of grid points is fixed for each mesh, so is p. This is in contrast to the usual mesh, where no specific value of p is chosen. Without such special relocation of grid points, it is normally considered that most curvilinear mesh has a geometric approximation error. The critical effects of the geometric approximation error for the accuracy of the numerical solution are considered as follows.

The first effect is the change of metric identity to satisfy the following equality for a divergence-free vector \mathbf{F} on a curved domain Ω [6, 12].

$$\int_{\Omega} \nabla \cdot \mathbf{F} dx = \sum_{i=1}^{2} (J \nu_i F_i)_{;i} = 0,$$

where ν_i is the *i*th tangent vector of the curved coordinate axis ξ^i , J is the Jacobian, and; i is the covariant differentiation with respect to axis ξ^i . In addition to the changes of ν_i and ξ^i which will be described in details as the next effect, the change of the Jacobian J is caused by geometric approximation error to deteriorate the metric identity. However,

^{*}This research was supported by Brain Research Program through the National Research Foundation of Korea(NRF) funded by the Ministry of Science and ICT(NRF-2017M3C7A1049051)

the mathematical or computational methods to redefine the Jacobian by disregarding geometric approximation error would be challenging.

The second effect is the change of the tangent vector v_i and consequently, the surface normal vector k due to the modified curved axis ξ^i . This leads to the immediate projection of the initial vector, which is defined in the original domain. Thus, the magnitude and direction of the vector could be altered because the vector lies on a different tangent plane. More importantly, the covariant derivative of the vector changes on the mesh with geometric approximation error. For example, vectors on the protruded grid points from the original domain may generate a spurious divergence, which should not be generated by vectors in the original domain. Also, the modified direction of the tangent vector could yield a different magnitude and direction of differential operators such as divergence and curl.

This paper proposes a novel scheme mainly to cancel the second effect by geometric approximation error. The tangent vector of the original domain is retrieved, and the spurious divergence by the protruded grid points beyond the original domain is removed. Thus, the proposed scheme achieves better accuracy and conservational properties, particularly in mass and energy. However, this scheme is restricted for the case when the first effect of geometric approximation error remains relatively negligible, i.e., the variation of the Jacobian J is relatively small such that the metric identity approximately holds.

The order of this paper is organized as follows. Chapter 2 explains the changes of divergence by geometric approximation error. Chapter 3 proposes a mathematical scheme to remove the spurious divergence by geometric approximation error. In Chapter 4, geometry-aligned moving frames are explained to construct LOCAL and LOCSPH moving frames, depending on the alignment of the surface normal vector. Chapter 5 and 6 demonstrate the numerical tests of static divergence and curl on the sphere along with corresponding partial differential equations such as conservational laws and Maxwell's equations. Chapter 7 displays several numerical tests to show the accuracy of the proposed scheme, particularly in the conservation of mass and energy. Discussion is followed in Chapter 8.

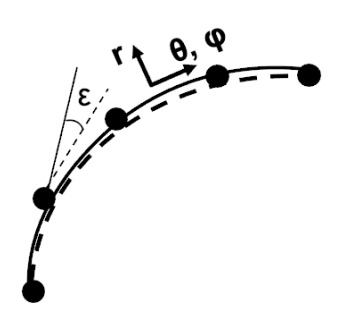


Figure 1: Illustration of geometric approximation error and the angle ε . Dashed line = surface of the target geometry Ω , solid line = surface of the domain Ω^{ε} . The end points corresponding to the vertices are on the curved domain Ω , but not the intermediate points.

2 Divergence by geometric approximation error

Suppose that Ω is the curved domain. Suppose that the tessellation of the domain is obtained as

$$\Omega = \cup_e \Omega_e$$
, where $\Omega_i \cap \Omega_j = \emptyset$

and all the vertices lie on Ω . If the surface is tessellated with the Euclidean elements with straight edges, such as regular triangles or quadrilaterals, the numerical solution with p=1 does not require additional points on the domain. For curvilinear meshes where curved edges are approximated with a polynomial of q>2, the numerical solution of p>2 places additional grid points on each element other than the vertices. Some of the additional grid points of the curvilinear mesh for p>2 are not on Ω but are slightly misplaced from it. This approximation causes a very small geometric approximation error which is mostly related to p-approximation. Let us denote the element of the domain with a geometric approximation error of ε as Ω_e^ε . Also, use the superscript ε to represent the corresponding quantity, i.e., a vector or a differential operator, lies on Ω^ε . Applying the divergence theorem to an arbitrary vector \mathbf{v}^ε on Ω_e^ε yields

$$\int_{\Omega_{\varepsilon}^{\varepsilon}} \nabla^{\varepsilon} \cdot \mathbf{v}^{\varepsilon} d\mathbf{x} = \int_{\partial \Omega_{\varepsilon}^{\varepsilon}} \mathbf{n}^{\varepsilon} \cdot \mathbf{v}^{\varepsilon} ds. \tag{2.1}$$

The flux that enters through the boundaries of the domain is the divergence of the vector. It is often identified as the source of the flow. One problem with the above equality is that the geometric error also contributes to the magnitude

of the divergence and consequently to the changes of conservational properties related to the velocity vector such as mass or energy.

For example, consider the spherical shell of radius r with the metric $ds^2 = r^2 d\theta^2 + r^2 \sin^2 \theta d\phi^2$. Consider a velocity vector \mathbf{v} on this sphere such that the velocity is expanded by the tangent vectors of the two axes of the surface such as $\mathbf{v} = v_\theta \boldsymbol{\theta} + v_\phi \boldsymbol{\phi}$. The exact divergence of this vector on Ω is given as

$$\nabla \cdot \mathbf{v} = \frac{1}{r} \frac{\partial v_{\theta}}{\partial \theta} + \frac{1}{r \sin \theta} \frac{\partial v_{\phi}}{\partial \phi}.$$

For the domain Ω^{ε} where the grid points other than the vertices do not lie on the exact sphere of radius r, the r component of the vector is not negligible, thus the velocity vector \mathbf{v}^{ε} on Ω^{ε} is expressed as

$$\mathbf{v}^{\varepsilon} = v_{\pi}^{\varepsilon} \mathbf{r} + (v_{\theta} - v_{\theta}^{\varepsilon}) \boldsymbol{\theta} + (v_{\phi} - v_{\phi}^{\varepsilon}) \boldsymbol{\phi}, \tag{2.2}$$

where v_r^{ε} , v_r^{ε} , and v_r^{ε} are created by the geometric approximation error. Suppose that the geometric error is sufficiently small and consequently the vector components created by the geometric approximation error are correspondingly sufficiently small. The velocity vector \mathbf{v}^{ε} is still on the surface, thus if two independent tangent vectors of Ω^{ε} are derived such as $\mathbf{e}_1^{\varepsilon}$ and $\mathbf{e}_2^{\varepsilon}$, then \mathbf{v}^{ε} is expressed on the surface such as $\mathbf{v}^{\varepsilon} = v_1 \mathbf{e}_1^{\varepsilon} + v_2 \mathbf{e}_2^{\varepsilon}$. However, $\mathbf{e}_1^{\varepsilon} \cdot \mathbf{r}$ or $\mathbf{e}_2^{\varepsilon} \cdot \mathbf{r}$ is not trivial because of the geometric approximation error. Then, the divergence of Eq. (2.2) is expressed as

$$\nabla \cdot \mathbf{v}^{\varepsilon} = \frac{1}{r^2} \frac{\partial (r^2 v_r^{\varepsilon})}{\partial r} + \frac{1}{r} \frac{\partial}{\partial \theta} (v_{\theta} - v_{\theta}^{\varepsilon}) + \frac{1}{r \sin \theta} \frac{\partial}{\partial \phi} (v_{\phi} - v_{\phi}^{\varepsilon}).$$

If the tangent vector of the protruded grid points are aligned parallel to the curved domain Ω , then it is widely accepted that the value of the grid points are extended in the direction of the surface normal vector. Thus, no additional error is generated. If additional grid points causing the geometric error increases gradually make an angle of ε with respect to the exact surface as shown in Fig. 1, then the velocity vector would be projected on the angled surface to induce the changes of v_{θ}^{ε} and v_{ϕ}^{ε} such as

$$||v_{\theta}^{\varepsilon}|| = ||\mathbf{v}^{\varepsilon}|| \cos \varepsilon \approx \mathcal{O}(\varepsilon^2).$$

The same error bound for v_{ϕ}^{ε} . However, the change of v_r^{ε} is of a lower order, equivalent to

$$\|v_r^{\varepsilon}\| = \|\mathbf{v}^{\varepsilon}\| \sin \varepsilon \approx \mathcal{O}(\varepsilon).$$
 (2.3)

For a small ε , the error caused by the geometric approximation error is thus dominated by v_r^{ε} and its derivative along the surface normal direction. It means that suppressing the divergence caused by the geometric approximation error can improve the accuracy significantly. Therefore, the goal of the scheme is to separate the divergence caused by geometric approximation error from the exact divergence of the velocity vector on a curved element with a geometric approximation error $\Omega_{\varepsilon}^{\varepsilon}$ as follows.

$$\int_{\Omega_{\varepsilon}^{\varepsilon}} \nabla_{S} \cdot \mathbf{v}^{\varepsilon} d\mathbf{x} + \int_{\Omega_{\varepsilon}^{\varepsilon}} \nabla_{G} \cdot \mathbf{v}^{\varepsilon} d\mathbf{x} = \int_{\partial \Omega_{\varepsilon}^{\varepsilon}} \mathbf{n}^{\varepsilon} \cdot \mathbf{v}^{\varepsilon} ds, \tag{2.4}$$

where ∇_{G} is the divergence operator caused by the geometric approximation error and ∇_{S} is the difference between the total divergence and ∇_{G} . In the previous example, ∇_{G} corresponds to the derivatives of $r^{2}v_{r}^{\varepsilon}$ along the surface normal direction.

3 Divergence by Curl Theorem

Consider the following Stokes theorem on the curved element Ω_e^{ε} as follows.

$$\iint_{\Omega_{\varepsilon}^{\varepsilon}} (\nabla^{\varepsilon} \times \mathbf{F}^{\varepsilon}) \cdot d\mathbf{S}^{\varepsilon} = \oint_{\partial \Omega_{\varepsilon}^{\varepsilon}} \mathbf{F}^{\varepsilon} \cdot d\ell^{\varepsilon}. \tag{3.1}$$

For the curved element Ω_e^{ε} , two orthonormal basis vectors can be chosen such as $\mathbf{e}_1^{\varepsilon}$ and $\mathbf{e}_2^{\varepsilon}$. Then, the surface normal vector can be derived as $\mathbf{k}^{\varepsilon} = \mathbf{e}_1^{\varepsilon} \times \mathbf{e}_2^{\varepsilon}$. Let us first consider the basis vector $\mathbf{e}_i^{\varepsilon}$ lying on the element Ω_e^{ε} .

By substituting $\mathbf{F}^{\varepsilon} = \mathbf{k}^{\varepsilon} \times \mathbf{v}^{\varepsilon}$ into Eq. (3.1), we obtain

$$\iint_{\Omega_{e}^{\varepsilon}} (\nabla^{\varepsilon} \cdot \mathbf{v}^{\varepsilon}) dA - \iint_{\Omega_{e}^{\varepsilon}} \mathcal{G}(\mathbf{k}^{\varepsilon}, \mathbf{v}^{\varepsilon}) dA = \oint_{\partial \Omega_{e}^{\varepsilon}} \mathbf{n}^{\varepsilon} \cdot \mathbf{v}^{\varepsilon} ds, \tag{3.2}$$

where $\mathbf{n}^{\varepsilon} = d\boldsymbol{\ell}^{\varepsilon} \times \mathbf{k}^{\varepsilon}$. The new function $\mathcal{G}(\mathbf{k}, \mathbf{v})$ is defined as follows.

$$G(\mathbf{k}, \mathbf{v}) = \mathbf{k} \cdot (\mathbf{k} \cdot \nabla) \mathbf{v} - \mathbf{k} \cdot (\mathbf{v} \cdot \nabla) \mathbf{k}, \tag{3.3}$$

where each vector differential operations can be computed as follows.

$$\mathbf{C} \cdot (\mathbf{A} \cdot \nabla) \mathbf{B} = \mathbf{C} \cdot [\mathbf{A} \cdot \nabla B_x \ \mathbf{A} \cdot \nabla B_y \ \mathbf{A} \cdot \nabla B_z]^T.$$

The function $\mathcal{G}(\mathbf{k}, \mathbf{v})$ approximately measures the variation of \mathbf{v} with respect to \mathbf{k} and vice versa. The first component of $\mathcal{G}(\mathbf{k}, \mathbf{v})$ in Eq. (3.3) is always negligible if \mathbf{v} lies on the tangent plane of Ω^{ε} and \mathbf{k} is orthogonal to it. This is because the gradient by the orthonormal basis \mathbf{e}_i lies on the tangent plane and is orthogonal to the surface normal vector \mathbf{k}^{ε} . For other cases such that \mathbf{v} and \mathbf{k} are not coincident with Ω , this component could be not negligible. The second component of $\mathcal{G}(\mathbf{k}, \mathbf{v})$ in Eq. (3.3) represents the variation of the surface normal vector with respect to the velocity vector \mathbf{v}^{ε} . This component is not necessarily zero because of mesh error. This quantity usually converges as the space discretization increases. Particularly for a high-order method such as spectral h/p method, $\mathbf{k} \cdot (\mathbf{v} \cdot \nabla) \mathbf{k}$ converges exponentially to zero as will be validated in the following test problems in the next sections.

Eq. (3.2) implies that the flow through the boundaries contributes to the divergence $\nabla^{\varepsilon} \cdot \mathbf{v}^{\varepsilon}$ and the geometric source $\mathcal{G}(\mathbf{k}, \mathbf{v})$. The divergence operator $\nabla^{\varepsilon} \cdot$ is also defined on the approximated surface $\Omega_e^{\varepsilon} e$, or more accurately on the tangent plane of Ω^{ε} . Thus, the divergence $\nabla^{\varepsilon} \cdot \mathbf{v}^{\varepsilon}$ in Eq. (3.2) computes all the divergence by the velocity vector \mathbf{v}^{ε} on Ω_e^{ε} . However, it also includes the additional divergence by the inaccurate geometric approximation. Because $\mathcal{G}(\mathbf{k}, \mathbf{v})$ partly represents the additional divergence by geometric approximation error, the difference of these two divergences is closer to the net flux of the flow, i.e.,

Net flux
$$\approx \nabla^{\varepsilon} \cdot \mathbf{v}^{\varepsilon} - \mathcal{G}(\mathbf{k}, \mathbf{v})$$
.

Thus, $\mathcal{G}(\mathbf{k}, \mathbf{v})$ is called *spurious divergence* by geometric approximation error.

In the previous example of Eq. (2.2), the velocity vector \mathbf{v}^{ε} on Ω_{e}^{ε} has a very small component v_{r}^{ε} along the surface normal vector \mathbf{k} of the curved domain Ω . Moreover, the gradient defined by the two orthonormal bases $\mathbf{e}_{i}^{\varepsilon}$ also has a component along the direction of \mathbf{k} . Thus, the surface normal vector of Ω_{e}^{ε} , or \mathbf{k}^{ε} , has a small component orthogonal to \mathbf{k} . Therefore, it is possible that $(\mathbf{v}^{\varepsilon} \cdot \nabla)\mathbf{k}^{\varepsilon}$ is not trivial, particularly when the space discretization is relatively coarse. However, it converges to zero as the space discretization increases. The non-negligible spurious geometric source $\mathcal{G}(\mathbf{k}, \mathbf{v})$ independent of p would emerge, particular when the vector is not on the tangent plane of Ω_{e}^{ε} .

4 Geometrically-aligned moving frames

On the element with a geometric approximation error Ω_e^{ε} , vectors and the gradients in the numerical scheme are defined on the plane expanded by the two basis vectors. This plane is generally oblique to the tangent planes of Ω . Thus, error occurs in the representation of the velocity vector and its differentiation. However, the surface normal vector is always orthogonal to the velocity vector and the tangent plane of Ω_e^{ε} . Thus, $\mathbf{k}^{\varepsilon} \cdot (\mathbf{k}^{\varepsilon} \cdot \nabla) \mathbf{v}^{\varepsilon}$ is close to the machine precision, though $\mathbf{k}^{\varepsilon} \cdot (\mathbf{v}^{\varepsilon} \cdot \nabla) \mathbf{k}^{\varepsilon}$ could be non trivial in a coarse mesh. However, $\mathbf{k}^{\varepsilon} \cdot (\mathbf{v}^{\varepsilon} \cdot \nabla) \mathbf{k}^{\varepsilon}$ decreases as p increases. Consequently, the magnitude of $\mathcal{G}(\mathbf{k}, \mathbf{v})$ is sufficiently small when refinement increases, i.e., h decreases or p increases.

Consider the orthonormal basis vectors \mathbf{e}_i , or moving frames, of the curved domain Ω . The velocity vector defined on Ω is fully expanded by \mathbf{e}_i without any projection error. Consider a vector $\mathbf{F} = \mathbf{k} \times \mathbf{v}$ where \mathbf{k} is the surface normal vector \mathbf{k}^{ε} of Ω and the velocity vector defined as $\mathbf{v} = v^1 \mathbf{e}_1 + v^1 \mathbf{e}_2$. Consequently, the vector \mathbf{F} also lies on the tangent plane of Ω . However, the surface normal vector of Ω_e^{ε} is not orthogonal to \mathbf{e}_i and the velocity vector \mathbf{v} . Consequently, $\mathbf{k} \cdot (\mathbf{k} \cdot \nabla) \mathbf{v}$ is significantly large and does not converge as p increases. The magnitude of $\mathbf{k} \cdot (\mathbf{v} \cdot \nabla) \mathbf{k}$ remains the same as that with $\mathbf{e}_i^{\varepsilon}$ for Ω_e^{ε} . Consequently, the magnitude of \mathcal{G} is also significant. The basis vectors \mathbf{e}_i of Ω for Ω_e^{ε} are called geometry-aligned moving frames to stress out that the moving frames \mathbf{e}_i represent the geometry of the original domain Ω .

Geometry-aligned moving frames would be particularly useful when the exact solution or any parameter of equations for the divergence is given in the specific coordinate system, such as the spherical coordinate axis. One main reason that it is not favored is that the numerical scheme with geometry-aligned moving frames yields more error, particularly in conservational properties. If moving frames lies on the different tangent plane than one of the curved element Ω_e^{ε} , the scheme generally produces a larger conservational error or even more significant discretization error. The proposed scheme with geometry-aligned moving frames in Eq. (3.2) suggests an accurate numerical scheme to yield better accuracy and overall accurate conservational properties, as will be demonstrated in the computational tests in the next sections.

4.1 Two types of LOCAL moving frames

In the following test problems, two types of local orthonormal bases, known as *moving frames*, are used. The first is based on the orthonormal bases that lie on the tangent plane of the surface, which is called as *LOCAL* moving frames

[4]. In the context of the element-wise mapping from the standard element to the curved element of the domain, the construction of these bases can be achieved easily by using the differentiation of the map as follows. Suppose s_1 and s_2 be the two independent axes of the standard element of unit length Ω^s . Suppose a map $\mathbf{c}(s_1, s_2)$ from Ω^s to a curved element Ω^e . Note that the map $\mathbf{c}(s_1, s_2)$ represents the coordinate of the curved element Ω^e and the Jacobian is not constant.

This map corresponds the grid points and the tangent vectors of Ω^s to those of Ω^e , respectively. If $\partial/\partial s_i$ is represented as the tangent vector of the domain Ω^s , then the map also sends these tangent vectors onto Ω^e as follows.

$$\mathbf{c}\left(\frac{\partial}{\partial s_i}\right) = \frac{\partial \mathbf{c}}{\partial s_i} \in \Omega^e,$$

where the equality holds by the law of vector map. The above equation implies that the tangent vector of the curved element is obtained by differentiating the map $\mathbf{c}(s_1, s_2)$ with respect to the axis s_i , i=1,2. The orthonormalization of the derived two tangent vectors, which are not necessarily orthonormal, creates the local orthonormal basis \mathbf{e}_1 and \mathbf{e}_2 . The differentiability of these bases is guaranteed by the sufficient smoothness of the map $\mathbf{c}(s_1, s_2)$. The third basis \mathbf{e}_3 is obtained by the curl of the two basis vectors. The obtained LOCAL moving frames are generally discontinuous across the interfaces of the elements. The additional process could be applied, though it is not necessary, to construct more Euclidean moving frames by comparing the divergence of \mathbf{e}_1 along each edge direction [4].

The LOCAL moving frames coincide with the local shape of the surface and are thus critically affected by geometric approximation error. This means that e_3^ε and k has a very small angle difference. This angle difference can be used as a quantized value to represent the geometric approximation error. Geometry-aligned moving frames could be continuous as the spherical coordinate axis. However, it would be more advantageous to have discontinuous frames across the interfaces of elements to avoid the geometric singularities, particularly for a closed surface such as the sphere.

Then, discontinuous geometry-aligned moving frames can be conveniently obtained from LOCAL moving frames. The first step is to replace \mathbf{e}_3 with $\mathbf{k}/\|\mathbf{k}\|$. The second step is to project \mathbf{e}_1 and \mathbf{e}_2 onto the new tangent space which has $\mathbf{k}/\|\mathbf{k}\|$ as \mathbf{e}_3 . Another orthonormalization of the basis vectors creates a set of LOCAL moving frames without geometric approximation error. When the surface normal vector is the same as that of the sphere with unit length, we call it as *LOCSPH* (short for LOCAL SPHERE) moving frames in this paper.

For the test problems in the next sections, the following spherical mesh is used. The maximum edge length is h=0.4 with 480 curved elements. Each edge has the maximum order of polynomial of 3. Table 1 shows the failure of the convergence of mesh error as p increase due to geometric approximation error.

p	2	3	4	5	6
_	2.0497e-05 7.565e-05				

Table 1: For the exact radius r_{exact} of the domain, mesh error in L_2 is defined as $\sqrt{\sum_{i=1}^{N} (r_{\text{exact}} - r_i)^2/N}$ for all the indices i of the total N grid points. Mesh error in L_{inf} is defined as $\max_i ||r_{\text{exact}} - r_i||$.

5 Divergence Test

Consider two static divergence tests on the sphere of unit length. Let $x = \sin \theta \cos \phi$, $y = \sin \theta \sin \phi$, and $z = \cos \theta$. Expand the velocity vector in the spherical coordinate axis such as $\mathbf{v} = v_{\theta} \boldsymbol{\theta} + v_{\phi} \boldsymbol{\phi}$. The first test adapts the velocity vector \mathbf{v} defined as follows.

$$v_{\theta} = 1/\sin\theta, \quad v_{\phi} = 1.0.$$

The second test uses the well-known Rossby-Haurwitz flow defined such as

$$v_{\phi} = \omega \sin \theta + K \sin^3 \theta (4\cos^2 \theta - \sin^2 \theta) \cos 4\phi,$$

$$v_{\theta} = -4K \sin^3 \theta \cos \theta \sin 4\phi,$$

where $\omega = K = 7.848 \times 10^{-6} \ s^{-1}$. The divergence of the both flows on the sphere is zero, satisfying the metric identities as follows.

$$\int_{S^2} \nabla \cdot \mathbf{v}^i = 0, \quad i = 1, 2.$$

By using Eq. (3.2), a discontinuous Galerkin scheme for the above divergence with respect to a test function φ is expressed as

$$\int_{S^2} (\nabla \cdot \mathbf{v}) \varphi dA = -\int_{S^2} \nabla \varphi \cdot \mathbf{v} dA + \int_{\partial S^2} (\mathbf{n} \cdot \mathbf{v}^*) \varphi d\ell - \int_{S^2} \mathcal{G}(\mathbf{e}^3, \mathbf{v}) \varphi dA, \tag{5.1}$$

where * represents the corresponding quantity is the numerical flux at the interfaces. The upwind flux is chosen for its accurate performance.

Fig. 2b displays that the second component $\mathbf{k} \cdot (\mathbf{v} \cdot \nabla) \mathbf{k}$ exponentially converges to zero as p increases. Therefore, this component in \mathcal{G} is negligible in a sufficiently fine resolution. However, the magnitude of the first component of \mathcal{G} , or $\mathbf{k} \cdot (\mathbf{k} \cdot \nabla) \mathbf{v}$, is approximately constant. This component is significantly large, particularly when moving frames do not lie on the tangent plane of Ω_e^{ε} such as the LOCSPH scheme. The different magnitudes of \mathcal{G} for the LOCAL and LOCSPH schemes are well presented in Fig. 2a. The positive magnitude implies the scheme with \mathcal{G} is more accurate.

Table 2 shows the comparison between the L_2 errors between the scheme of Eq. (5.1) with the two different local frames, LOCAL and LOCSPH moving frames. In Table 2, LOCSPH moving frames show better accuracy than LOCAL moving frames, particularly as p increases. For test 1, the L_2 error of LOCAL moving frames is stagnant around $3.94\mathrm{e}{-6}$, possibly due to mesh error. However, the L_2 error of LOCSPH moving frames converges up to $2.98\mathrm{e}{-7}$. This error is less than 10% of the error of LOCAL moving frames. For test 2, the L_2 error of LOCAL moving frames stagnates around $1.49\mathrm{e}{-06}$, whereas the L_2 error of LOCSPH moving frames converges up to $1.47\mathrm{e}{-0.7}$.

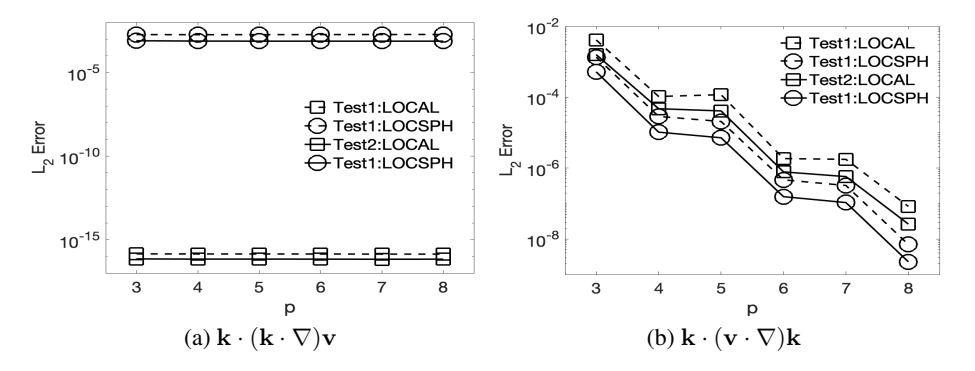


Figure 2: Convergence of \mathcal{G} for static divergence test. For test 1, $\mathbf{k} \cdot (\mathbf{k} \cdot \nabla) \mathbf{v}$ is approximately constant independent of p as 1.4e-16 and 1.8e-3 for LOCAL and LOCSPH moving frames, respectively. For test 2, it is approximately constant as 6.9e-17 and 7.4e-4 for LOCAL and LOCSPH moving frames, respectively. $\mathbf{k} \cdot (\mathbf{v} \cdot \nabla) \mathbf{k}$ exponentially converges to zero as p increases for test 1 and test 2 in LOCAL and LOCSPH moving frames.

Test 1			Tes	Test 2		
p	LOCAL	LOCSPH	LO	CAL	LOCSPH	
3	2.24e-04	2.24e-04	4.3	3e-05	4.32e-05	
4	2.10e-05	2.12e-05	4.4	2e-06	3.98e-06	
5	6.98e-06	6.26e-06	1.6	7e-06	4.85e-07	
6	4.12e-06	1.97e-06	1.4	8e-06	1.62e-07	
7	3.94e-06	3.97e-07	1.4	9e-06	1.49e-07	
8	3.94e-06	2.98e-07	1.5	3e-06	1.47e-07	

Table 2: Static divergence test: L_2 error for test 1 and test 2.

5.1 Conservational laws

For a constant velocity vector on the sphere, the following conservational laws is considered.

$$\frac{\partial u}{\partial t} + \nabla \cdot (u\mathbf{v}) = 0, \quad \mathbf{v} \in S^2.$$
 (5.2)

Then, the weak formulation of the above conservational law is obtained as

$$\int_{S^2} \frac{du}{dt} \varphi - \int_{S^2} \nabla \varphi \cdot \mathbf{v} u dA + \int_{\partial S^2} (\mathbf{n} \cdot \mathbf{v}^*) u \varphi d\ell - \int_{S^2} \mathcal{G}(\mathbf{e}^3, u \mathbf{v}) \varphi dA = 0,$$
(5.3)

To test the above conservational laws, a smooth cosine bell is advected around the sphere. Please refer to the following references for the detailed description of the test [2, 11, 16]. The original problem is to rotate the bell just one time. In this test, we rotate it up to ten times to observe the significant changes of the overall error and conservational error. Time is marched with the step size of 1.0e-04 by an explicit fourth-order Runge-Kutta scheme. The cosine bell is rotated at the angle of $\pi/4$ with respect to the axis of the poles.

Fig. 3 presents error convergences for the cosine bell test problem by Eq. (5.3). Fig. 3a shows that the overall error of LOCSPH with $\mathcal G$ increases as time increases. The differences of the LOCAL and LOCSPH schemes without $\mathcal G$ are presented with the dashed circle (Δ LOCAL) and dashed triangle(Δ LOCSPHnoG), respectively. At T=10.0, the difference is approximately 0.0394% and 0.0198%, and at T=20.0, the difference is approximately 0.0568 and 0.0224 for the LOCAL and LOCSPH schemes without $\mathcal G$, respectively.

Fig. 3b shows the mass conservational error of LOCSPH with $\mathcal G$ and its differences to other schemes. These Figures validate the better accuracy of LOCSPHwithG in Eq. (5.3) for conservational laws, in overall error, and conservational error. At T=10.0, the difference is approximately 12.0%, and at T=20.0, the difference is approximately 35.8% for LOCSPH without $\mathcal G$. Conservational error of LOCSPH with $\mathcal G$ is less than a thousand times than that of the LOCAL scheme. Therefore, Fig. 3 demonstrates the accuracy in the overall error and particularly conservational error.

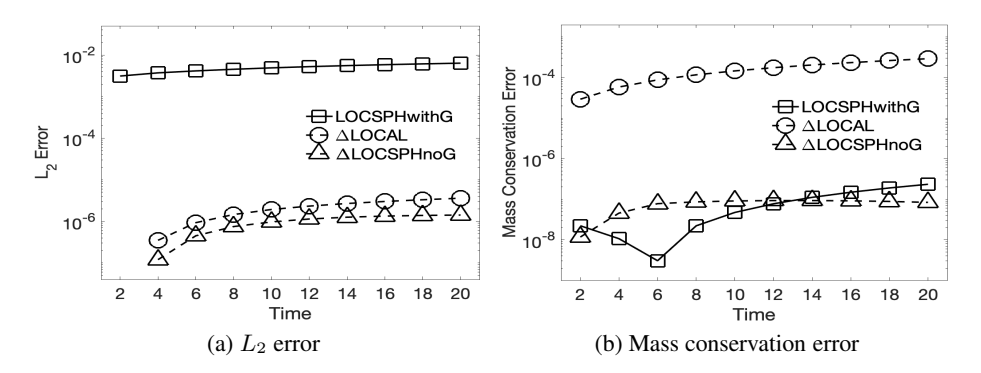


Figure 3: Conservational laws: error slowly increases as time increases for p=5. Every T=2 completes one turn around the great circle. Solid line corresponds each error of LOCSPH with \mathcal{G} (LOCSPHwithG). Dashed lines are error difference to LOCSPH without \mathcal{G} , or Δ LOCSPHnoGA = LOCSPHnoGA - LOCSPHwithG, and difference to that of the LOCAL scheme, or Δ LOCAL = LOCAL - LOCSPHwithG.

6 Curl Test

The curl tests for the curl with respect to the surface normal direction $(\nabla \times \mathbf{v}) \cdot \mathbf{k}$ are similar to the divergence tests. For the first test, the velocity vector \mathbf{v} is introduced as

$$v_{\theta} = 1.0, \quad v_{\phi} = 1/\sin \theta.$$

For the second test, a flipped Rossby-Haurwitz flow between the θ -axis and ϕ axis is used, which is defined such as

$$v_{\theta} = \omega \sin \theta + K \sin^{3} \theta (4 \cos^{2} \theta - \sin^{2} \theta) \cos 4\phi,$$

$$v_{\phi} = 4K \sin^{3} \theta \cos \theta \sin 4\phi,$$

where ω and K are the same as that of the divergence test. Then, the both flows are curl-free to have the following equality

$$\int_{\Omega} (\nabla \times \mathbf{v}) \cdot \mathbf{k} \varphi dA = 0. \tag{6.1}$$

Geometric effects on $(\nabla \times \mathbf{v}) \cdot \mathbf{k}$ are more complicated than the divergence of a vector because the magnitude of the curl only is measured along the surface normal vector. For example, the LOCAL and LOCSPH have different surface

normal direction when their tangent plane could be different. A discontinuous Galerkin scheme to compute Eq. (6.1) is given as

$$\int_{\Omega} (\nabla \times \mathbf{v}) \cdot \mathbf{e}_{3} \varphi dA = -\int_{\Omega} \nabla \varphi \cdot \tilde{\mathbf{v}}^{c} dA + \int_{\partial \Omega} (\mathbf{n} \cdot \tilde{\mathbf{v}}^{c*}) \varphi d\ell
+ \int v^{i} \mathbf{e}_{i} \cdot (\nabla \times \mathbf{e}_{3}) \varphi dx + \int_{\Omega} \mathcal{G}(\mathbf{e}^{3}, \tilde{\mathbf{v}}^{c}) \varphi dA,$$
(6.2)

where $\tilde{\mathbf{v}}^c \equiv -(\mathbf{v} \cdot \mathbf{e}_1)\mathbf{e}_2 + (\mathbf{v} \cdot \mathbf{e}_2)\mathbf{e}_1$. Table 3 confirms the convergence similar to the static divergence. The LOCSPH scheme is implemented with the \mathcal{G} component. The convergence of \mathcal{G} for the curl tests is similar to that of the static divergence test, as shown in Fig. 4.

Test 1			Test 2	Test 2		
p	LOCAL	LOCSPH	LOCAL	LOCSPH		
3	2.24e-04	2.24e-04	3.61e-05	3.69e-05		
4	1.97e-05	1.98e-05	4.12e-06	4.24e-06		
5	7.10e-06	7.22e-06	1.71e-06	1.79e-07		
6	4.202e-06	4.36e-06	1.51e-06	1.61e-07		
7	4.04e-06	4.28e-07	1.51e-06	1.62e-07		
8	4.04e-06	4.29e-07	1.52e-06	1.62e-07		

Table 3: Static curl test: L_2 error for LOCAL and LOCSPH moving frames versus p.

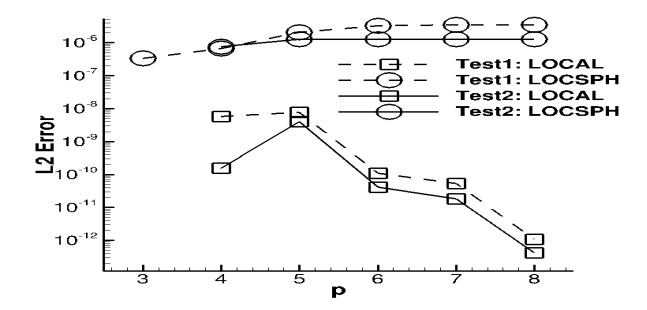


Figure 4: Convergence of \mathcal{G} for the static curl tests. \mathcal{G} is of a significant magnitude only for LOCSPH moving frames, independent of p. $\mathbf{k} \cdot (\mathbf{k} \cdot \nabla) \mathbf{v}$ is approximately constant as 1.72e-29 and 5.28e-6 with LOCAL and LOCSPH moving frames. Similarly, $\mathbf{k} \cdot (\mathbf{v} \cdot \nabla) \mathbf{k}$ exponentially converges as p increases.

6.1 Maxwell's equations

For time-dependent PDEs with the curl operator, Maxwell's equations are chosen as follows

$$\hat{\varepsilon} \frac{\partial \mathbf{E}}{\partial t} = \nabla \times \mathbf{H}, \quad \hat{\mu} \frac{\partial \mathbf{H}}{\partial t} = -\nabla \times \mathbf{E},$$
(6.3)

where **E** and **H** is the electric field and h-field, respectively. $\hat{\varepsilon}$ and $\hat{\mu}$ is the permittivity and permeability tensor, respectively. Consider transverse magnetic (TM) mode such that $\mathbf{H} = H^1\mathbf{e}_1 + H^2\mathbf{e}_2$ and $\mathbf{E} = E^3\mathbf{e}_3$. Transverse electric (TE) mode would yield the similar results. Then, the weak formulation of Maxwell's equations in Eq. (6.3) in the context of discontinuous Galerkin methods is given as follows. For i = 1, 2, we have

$$\int \mu^{i} \frac{\partial H^{i}}{\partial t} \varphi dx = \int \nabla \varphi \cdot \mathbf{E}_{i}^{*} dx - \int \mathbf{E} \cdot (\nabla \times \mathbf{e}_{i}) \varphi dx$$
$$- \int_{\partial \Omega} \mathbf{n} \cdot \widetilde{\mathbf{E}}_{i}^{*} \varphi ds - \int \mathcal{G}(\mathbf{E}_{i}^{*}) \varphi dx, \tag{6.4}$$

where $\mathbf{E} = E^3 \mathbf{e}_3$ and $\mathbf{E}_i^* = E^3 \mathbf{e}_{3i} = E^3 (\mathbf{e}_3 \times \mathbf{e}_i)$. The tilde sign implies that the corresponding quantity is approximated value at the boundary, called numerical flux. The permeability tensor is also decomposed into two

frames e^1 and e^2 such as $\hat{\mu} = \mu^1 e^1 + \mu^2 e^2$. The electric field is updated as follows.

$$\int \varepsilon^{3} \frac{\partial E^{3}}{\partial t} \varphi dx = \sum_{i=1}^{2} \left[-\int \nabla \varphi \cdot \mathbf{H}_{i}^{*} dx + \int \mathbf{H}^{i} \cdot (\nabla \times \mathbf{e}_{3}) \varphi dx + \int_{\partial \Omega} \mathbf{n} \cdot \widetilde{\mathbf{H}}_{i}^{*} \varphi ds + \int \mathcal{G}(\mathbf{H}_{i}^{*}) \varphi dx \right], \tag{6.5}$$

where $\mathbf{H}^i = H^i \mathbf{e}_i$ and $\mathbf{H}_i^* = H^i \mathbf{e}_{i3} = H^i (\mathbf{e}_i \times \mathbf{e}_3)$. For the test of this numerical scheme, the following test problem is adapted from ref. [3].

$$\frac{\partial \mathbf{H}}{\partial t} = -\nabla \times \mathbf{E} + \mathbf{F} \sin \omega t, \quad \frac{\partial \mathbf{E}}{\partial t} = \nabla \times \mathbf{H}, \tag{6.6}$$

where we let $\omega = \sqrt{2}$ and the solution of the above equations is given as

$$\mathbf{H}(\theta, \phi, t) = \mathbf{V}(\theta, \phi) \cos \omega t, \quad \mathbf{E}(\theta, \phi, t) = \frac{\zeta(\theta, \phi)}{\omega} \sin \omega t \mathbf{k},$$

where \mathbf{k} is the surface normal vector. The expression of other variables and the values of parameters are the same as described in ref. [3]. Time step is dt = 0.001 up to the final time T = 0.5. A classical Runge Kutta explicit time step is used for time marching. For the numerical flux, the efficient upwind flux is used [3].

Table 4 displays the accuracy of the three schemes and confirms again that the LOCSPH scheme shows the best accuracy. LOCAL moving frames yields the worst accuracy because the curl operator is computed by basis vectors oblique to the spherical coordinate axis due to geometric approximation error. Even with a high p>3, the L_2 error of LOCAL moving frames stagnates around 1.0e-4. Adapting LOCSPH moving frames improves accuracy, converging up to 6.86e-05. However, LOCSPH moving frames with $\mathcal G$ presents the best accuracy, which converges up to 4.30e-05.

Fig. 5 presents the initial shock of electromagnetic pulse and energy conservation error during the extremely low frequency (ELF) propagation on the sphere. The TM mode is chosen. As shown in Fig. 5a, a shock is initiated at $(1/\sqrt{2},0,1/\sqrt{2})$ to propagates infinitely between the initial point and antipode without losing energy. Energy conservation error for various schemes is shown in Fig. 5b. The LOCAL and LOCSPH schemes provide accurate conservation of energy. However, LOCSPH with $\mathcal G$ demonstrates the superior performance in the conservation of energy in Maxwell's equations. LOCSPH without $\mathcal G$ shows an erratic convergence as time marches. This occurs because moving frames used for the computation of the curl is also used for the decomposition of vector fields, for example, as shown in Fig. 6.4. Introducing two kinds of moving frames would eliminate this kind of erratic convergence and will be described in more detail in the next section.

p	LOCAL	LOCSPHnoG	LOCSPHwithG
1	3.20e-02	3.17e-02	3.07e-02
2	2.61e-03	2.62e-03	2.61e-03
3	5.72e-04	4.45e-04	4.31e-04
4	1.30e-04	6.92e-05	4.43e-05
5	1.53e-04	6.86e-05	4.30e-05

Table 4: Convergence of error for the problem Eq. (6.6).

7 Application to shallow water equations

An immediate application of the proposed scheme is the shallow water equations (SWEs) on the sphere given as follows

$$\frac{\partial H}{\partial t} + \nabla \cdot (H\mathbf{u}) = 0, \tag{7.1}$$

$$\frac{\partial H\mathbf{u}}{\partial t} + \nabla \cdot (H\mathbf{u}\mathbf{u}) + \frac{g}{2}\nabla H^2 = fH(\mathbf{u} \times \mathbf{k}) + gH\nabla H_0, \tag{7.2}$$

where η and u represent the free surface elevation, and the depth-averaged velocity. H_0 is the still water depth and $H = H_0 + \eta$ is the total water depth. f and g means the Coriolis parameter and the gravitational constant, respectively. Geometry-aligned moving frames for the SWEs have a different meaning than conservational laws or

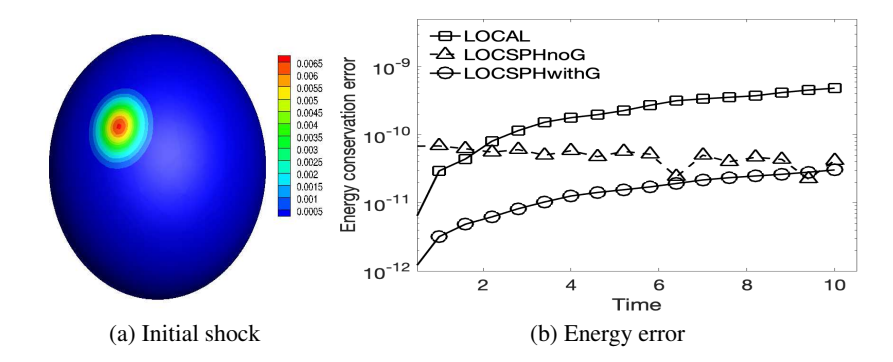


Figure 5: ELF propagation on the sphere and energy conservation error. TM mode.

Maxwell's equations. This is because the SWEs are not totally coordinate-independent. A component-wise expression of Eq. (7.2) for $\mathbf{u} = u\mathbf{e}_1 + v\mathbf{e}_2$ is obtained as follows.

$$\frac{\partial H\mathbf{u}}{\partial t} \cdot \mathbf{e}_1 + \nabla \cdot (Hu\mathbf{u}) + H\mathbf{u} \cdot \nabla \mathbf{e}_1 \cdot \mathbf{u} + \frac{g}{2} \nabla H^2 \cdot \mathbf{e}_1 = fHu + gH\nabla H_0 \cdot \mathbf{e}_1, \tag{7.3}$$

$$\frac{\partial H\mathbf{u}}{\partial t} \cdot \mathbf{e}_2 + \nabla \cdot (Hv\mathbf{u}) + H\mathbf{u} \cdot \nabla \mathbf{e}_2 \cdot \mathbf{u} + \frac{g}{2} \nabla H^2 \cdot \mathbf{e}_2 = -fHv + gH\nabla H_0 \cdot \mathbf{e}_2, \tag{7.4}$$

The above equations assumes the following zero tendency condition.

$$\mathbf{u} \cdot \nabla \mathbf{e}_i \cdot \mathbf{u} = 0, \qquad 1 \le i \le 2. \tag{7.5}$$

As moving frames are more Euclidean, the left-hand side of Eq. (7.5) is closer to zero for i=1,2. For the popular Williamson's tests, the zero tendency of the spherical coordinate should be satisfied by the spherical coordinate axis. The tendency is usually not incorporated into the numerical scheme of SWES, assumed to be zero or approximately negligible compared to discretization error. Consequently, changing the coordinate axis may change the accuracy, even on the perfect sphere.

In most numerical schemes [1, 5, 7, 10], the gradient of H^2 , or ∇H^2 , is computed in the weak formulation. However, $gH\nabla H_0$ is computed directly because the integration of part for $H\nabla H_0$ is impossible when H_0 is not a constant. For the given moving frames \mathbf{e}_i , the weak formulation of ∇H^2 can be computed similarly as the divergence as follows.

$$\int \nabla H^2 dx = \left(\int (\nabla H^2 \cdot \mathbf{e}_1) \mathbf{e}_1 \varphi dx \right) + \left(\int (\nabla H^2 \cdot \mathbf{e}_2) \mathbf{e}_2 \varphi dx \right), \tag{7.6}$$

where the directional derivative can be computed as follows.

$$\int \nabla H^{2} \cdot \mathbf{e}_{i} \varphi dx = -\int \nabla \varphi \cdot \mathbf{e}_{i} H^{2} dx - \int H^{2} (\nabla \cdot \mathbf{e}_{i}) \varphi dx + \int_{\partial \Omega} H^{2} (\mathbf{e}_{i} \cdot \mathbf{n}) \varphi ds + \int \mathcal{G}(H^{2} \mathbf{e}_{i}) \varphi dx$$

$$(7.7)$$

Because of the zero tendency requirement, two sets of moving frames are introduced for the scheme. The first moving frames, or e_i , is the LOCAL moving frames lying on the tangent plane of the domain. The second moving frames, or d_i , is introduced only to compute the weak formation of the divergence such as $\nabla \cdot H\mathbf{u}$, $\nabla \cdot Hu\mathbf{u}$, and $\nabla \cdot Hv\mathbf{u}$. The second moving frames are aligned along a specific coordinate axis with or without \mathcal{G} . Using Eq (5.1) and (7.7), we obtain the following weak formulation of geometry-aligned moving frames scheme with \mathcal{G} for the SWE equations in

the context of discontinuous Galerkin method.

$$\int \frac{\partial H}{\partial t} \varphi dx - \int H u^{d} \mathbf{d}^{1} \cdot \nabla \varphi dx - \int H v^{d} \mathbf{d}^{2} \cdot \nabla \varphi dx. \\
+ \int_{\partial \Omega} \widetilde{H} \tilde{\mathbf{u}} \cdot \mathbf{n} \varphi ds + \int \mathcal{G}(\mathbf{e}_{3}, H \mathbf{u}) \varphi dx. = 0, \tag{7.8}$$

$$\int \frac{\partial H u}{\partial t} \varphi dx + \int H \left(u \frac{\partial \mathbf{e}_{1}}{\partial t} + v \frac{\partial \mathbf{e}_{2}}{\partial t} \right) \cdot \mathbf{e}_{1} \varphi dx - \int H u (u^{d} \nabla \varphi \cdot \mathbf{d}^{1} + v^{d} \nabla \varphi \cdot \mathbf{d}^{2}) dx \tag{7.9}$$

$$- \int \frac{g H^{2}}{2} \nabla \varphi \cdot \mathbf{e}_{1} dx + \int_{\partial \Omega} \left[\widetilde{H} \widetilde{u}^{2} + \frac{g}{2} \widetilde{H}^{2} \right] (\mathbf{e}_{1} \cdot \mathbf{n}) \varphi dx - \int \frac{g H^{2}}{2} (\nabla \cdot \mathbf{e}_{1}) \varphi dx \tag{7.9}$$

$$+ \int \mathcal{G}(\mathbf{e}_{3}, H u \mathbf{u} + \frac{g}{2} H^{2} \mathbf{e}_{1}) \varphi dx = \int_{\Omega} f (H v) \varphi dx + \int_{\Omega} g H \nabla H_{0} \cdot \mathbf{e}_{1} \varphi dx.$$

$$\int \frac{\partial H v}{\partial t} \varphi dx + \int H \left(u \frac{\partial \mathbf{e}_{1}}{\partial t} + v \frac{\partial \mathbf{e}_{2}}{\partial t} \right) \cdot \mathbf{e}_{2} \varphi dx - \int H v (u^{d} \nabla \varphi \cdot \mathbf{d}^{1} + v^{d} \nabla \varphi \cdot \mathbf{d}^{2}) dx$$

$$- \int \frac{g H^{2}}{2} \nabla \varphi \cdot \mathbf{e}_{2} dx + \int_{\partial \Omega} \left[\widetilde{H} \widetilde{u}^{2} + \frac{g}{2} \widetilde{H}^{2} \right] (\mathbf{e}_{2} \cdot \mathbf{n}) \varphi dx - \int \frac{g H^{2}}{2} (\nabla \cdot \mathbf{e}_{2}) \varphi dx$$

$$+ \int \mathcal{G}(\mathbf{e}_{3}, H v \mathbf{u} + \frac{g}{2} H^{2} \mathbf{e}_{2}) \varphi dx = -\int_{\Omega} f (H u) \varphi dx + \int_{\Omega} g H \nabla H_{0} \cdot \mathbf{e}_{2} \varphi dx.$$

For the following numerical tests, the Lax-Friedrich flux is used for the numerical flux, and an explicit fourth-order Runge-Kutta scheme is used for time marching. The details of the test problems are well described in ref. [3, 16], thus will not be repeated in this paper.

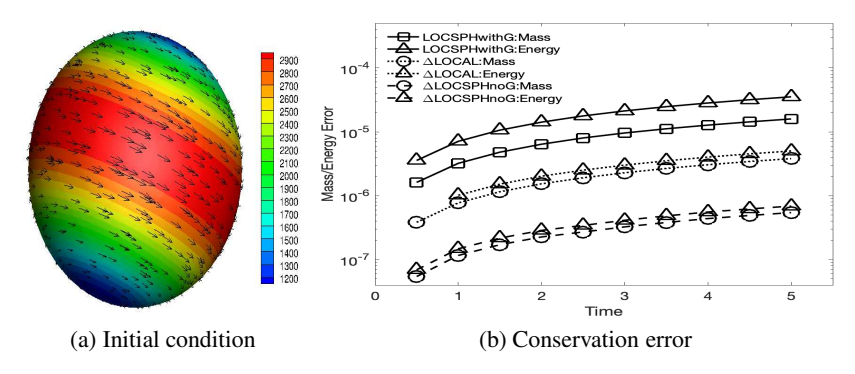


Figure 6: Steady zonal flow: Mass/Energy conservation error. $p=5.\ h=0.4$ with 480 elements. Measured up to T=5.0.

7.1 Steady Zonal flow

The first test is the steady zonal test with the constant free surface elevation and velocity vector over time. The angle of the velocity vector with respect to the polar axis is set as $\pi/4$. The still water depth (H_0) is chosen as 1.0, thus $\nabla H_0 = 0$. We let \mathbf{d}^i be LOCSPH moving frames when \mathbf{e}_i is the LOCAL moving frames. Define the following quantities for convenient comparisons between methods. Moving frames \mathbf{e}_i is chosen LOCAL moving frames. LOCAL_Mass and LOCAL_Energy correspond to the mass and energy conservation error of LOCAL moving frames for both \mathbf{e}_i and \mathbf{d}^i , respectively. LOCSPHnoG_Mass and LOCSPHnoG_Energy correspond to the mass and energy conservation error when \mathbf{d}^i is LOCSPH without \mathcal{G} , respectively. LOCSPHwithG_Mass and LOCSPHwithG_Energy correspond to the mass and energy conservation error when \mathbf{d}^i is LOCSPH with \mathcal{G} , respectively.

$$\Delta$$
LOCAL = LOCAL - LOCSPHwithG,
 Δ LOCSPHnoG = LOCSPHnoG - LOCSPHwithG.

The above quantities are positive if LOCSPHwithG_Mass and LOCSPHwithG_Energy are smaller than the error of LOCAL or LOCSPHwithG. Note that the plot is in log scale. Thus, the negative quantity does not appear in the plot.

Figure. 6 displays the increase of the mass and energy conservational error compared to the initial mass and energy. The LOCSPHwithG scheme confirms the least conservation error of mass and energy for h = 0.4 and p = 4. LOCAL

moving frames show the largest conservational error as its difference is denoted as the dotted line. The LOCSPHnoG scheme shows approximately 3.5% and 2.0% more conservational error than those of the LOCSPHwithG scheme in mass and energy, respectively. However, this better conservational accuracy of LOCSPHwithG is not always observed with all h and p, especially for a relatively much finer mesh or relatively much more coarse mesh. It is supposed that the better accuracy of LOCSPHwithG is observed only when the conservational error of the divergence component in Eqs. (7.1) and (7.2) is dominant.

7.2 Unsteady Zonal flow

One big difference between the unsteady zonal test and the steady zonal test is that the still surface elevation (H_0) is not constant as given as follows.

$$H_0(\theta) = \frac{133681}{r_a g} - \frac{10}{r_a g} - \frac{(\Omega_f \sin \theta)^2}{2g},$$

where r_a is the radius of the earth, g is the gravitational constant, and Ω_f is the Earth rotation frequency. Thus, $gH\nabla H_0\cdot \mathbf{e}_1$ should be computed directly because it cannot be computed in a weak form by the integration by part. Consequently, the spurious diffusion removal scheme cannot be applied to $H\nabla H_0$. Consequently, this component seems to be the main source of conservational error for this unsteady zonal flow. Fig. 7 confirms the better accuracy of the LOCSPH scheme with $\mathcal G$ compared to LOCAL moving frames. However, it also shows that the conservational accuracy obtained by $\mathcal G$ is quickly overwhelmed by the conservational error of $gH\nabla H_0\cdot \mathbf{e}_i$. The test is run up to T=0.5. The LOCSPH scheme with $\mathcal G$ does not show any better accuracy, approximately after T=0.35 in the same mesh as the steady zonal test.

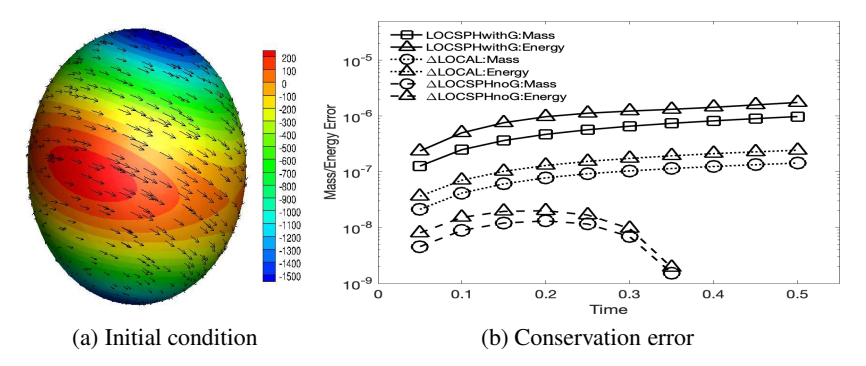


Figure 7: Unsteady zonal flow: Mass/Energy conservation error. p=5. h=0.4 with 480 elements. L_2 error for LOCAL and LOCSPH with G is 1.522e-05 and 5.186e-06, respectively.

7.3 Rossby-Haurwitz flow

The third test problem is the famous Rossby-Haurwitz flow on the sphere. There is no exact solution to this problem. However, the periodic distribution of the free surface elevation (η) and the velocity vector (\mathbf{u}) along the ϕ -axis rotate around the axis of the sphere. The conservational error of mass and energy is considered the most important measure to demonstrate the accuracy of the implemented numerical schemes. The initial distribution of η and \mathbf{u} is much more complicated than those of the steady zonal flow, as shown in Fig. 8. However, H_0 is constant, set as 1.0, and ∇H_0 is zero. Thus, the LOCSPH with $\mathcal G$ scheme can be implemented for better accuracy. Time is run up to 15 days.

Fig. 8 presents the mass and energy conservation error of the LOCSPHwithG scheme and its differences with the LOCAL and LOCSPHnoG schemes. The general behavior of the plots is similar to that of the steady zonal flows. The LOCSPHnoG scheme shows approximately 2.0% and 1.3% more conservational error than those of the LOCSPHwithG in mass and energy, respectively.

7.4 Perturbed unsteady jet flow

As the last test problem with the constant H_0 , the perturbed unsteady jet simulation is known to be one of the most challenging tests as the initial condition is presented in Fig. 9a. The length of the edge should be less than h=0.1, and consequently, the number of curved triangular elements are at least more than 10,000 for most of the numerical schemes. In such a refined mesh, the difference between the LOCAL and LOCSPH schemes is negligible. Thus, the

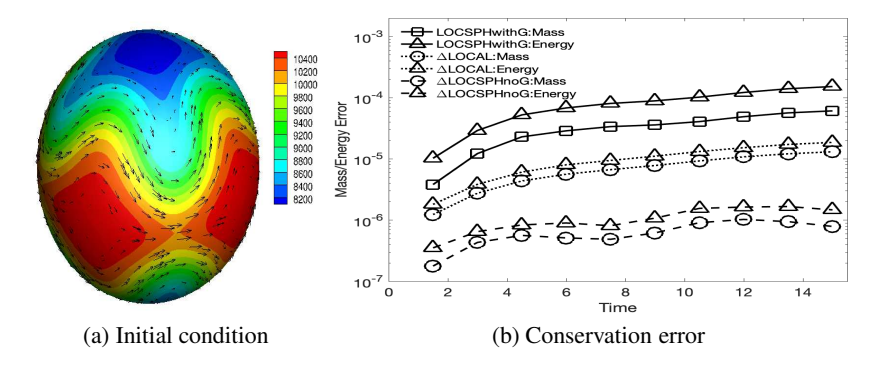


Figure 8: Rossy flow: Mass/Energy conservation error. p = 5. h = 0.4 with 480 elements.

LOCSPHwithG scheme does not always show a better accuracy because the error of the divergences such as $\nabla \cdot H\mathbf{u}$, $\nabla \cdot Hu\mathbf{u}$, and $\nabla \cdot Hv\mathbf{u}$ is not dominant in this refined mesh.

Thus, we test the same problem in a coarser mesh. Note that in this mesh, the signature pattern of the perturbed unsteady jet flow is not observed due to a large conservational error. However, it serves the purpose to observe the accuracy of the LOCSPHwithG scheme. Consider the same sphere as before with h=0.4 with 480 elements. The increasing mass and energy conservation error of the perturbed jet flow is shown in Fig. 9b. The LOCSPHwithG scheme shows the best accuracy. The LOCAL moving frames and the LOCSPHnoG scheme shows approximately a similar conservational error, which is approximately 1% larger than the LOCSPHwithG scheme.

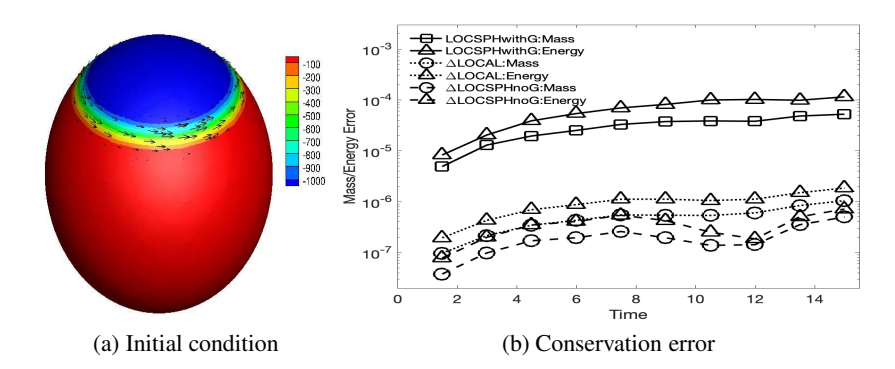


Figure 9: Perturbed unsteady jet: Mass/Energy conservation error. p = 5. h = 0.4 with 480 elements.

7.5 On an ellipsoid

Method of moving frames can be applied to any curved surface. Thus, Rossby-Haurwitz flow was tested again by the SWE equations in Eqs. (7.1) and (7.2) on an ellipsoid, geometrically similar to the Earth as an ellipsoid defined as follows [15].

$$\left(\frac{x}{a}\right)^2 + \left(\frac{y}{b}\right)^2 + \left(\frac{z}{c}\right)^2 = 1,$$

where a/c = b/c = 1.003364 and c is nondimensionalized as the unit length. The previous tests of SWEs are all derived on the sphere. Thus, we let moving frames for the divergence LOCSPH, same as the previous tests. Moving frames on the ellipsoid surface, called LOCAL ellipsoid, are closer to LOCAL moving frames of this domain. However, LOCAL ellipsoid does not satisfy the time-invariance conditions of SWEs for steady zonal and Rossby-Haurwitz flow. Thus, LOCAL ellipsoid produces more conservational error.

On the other hand, this could be considered as a more deformed domain than the previous cases. In the previous mesh with LOCSPH, the e_3 of LOCAL moving frames at vertices is sufficiently close to e_3 of LOCSPH moving frames. This is because all the vertices lie on the sphere. For the ellipsoidal domain, the e_3 of LOCAL moving frames could be significantly different from e_3 of LOCSPH moving frames. This is because even at the vertices, the surface normal

vector is not aligned along e_3 of LOCSPH moving frames. Thus, this test would show whether geometry-aligned moving frames can show a better accuracy for the discrete mesh of a slightly-deformed domain.

Fig. 10 displays the increase of the LOCSPHwithG scheme for the steady zonal flow and its differences to LOCAL and LOCSPHnoG schemes. For steady-state flow, as shown in Fig. 10a, the LOCSPHwithG scheme shows the best accuracy similar to the steady-state flow on the sphere. However, the error accuracy difference is much larger. The LOCAL scheme has approximately 50% and 30% more conservational error in mass and energy, respectively. The LOCSPHnoG scheme has approximately 20% and 10% more conservational error in mass and energy, respectively.

Fig. 10b displays the increase of mass and energy conservational error for Rossby-Haurwitz flow. For this complex flow, conservational error from other components seems to dominate in the beginning. Roughly after T=7, as more conservational error accumulates, the LOCSPHwithG scheme seems to successfully suppress the mass and energy conservational error from the divergence components to yield better accuracy than LOCAL and LOCSPHnoG schemes.

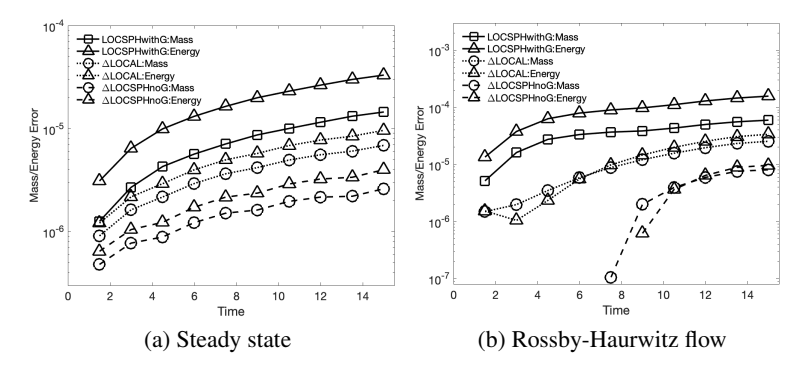


Figure 10: On the ellipsoid with the ratio of a/c = b/c = 1.003364 in $(x/a)^2 + (y/b)^2 + (z/c)^2 = 1$, approximately the same as the Earth, when c is normalized as the unit length. Mass/Energy conservation error. p = 5. h = 0.4 with 480 elements.

8 Discussion

This paper proposes a new scheme to improve the overall accuracy and particularly conservational error by aligning moving frames along the axis of the domain and removing spurious divergence. One drawback of the proposed scheme is that the spurious divergence computation could be expensive, considering that the obtained accuracy is less than 10% of that of the original scheme. When the governing equation has multiple components, it is difficult to know when the divergence error dominates the overall or conservational error. The proposed scheme also identifies the source of conservational error as the spurious divergence by geometric approximation error. This paper specifically implemented the proposed scheme using moving frames to differentiate and expand vectors on curved surfaces. However, a similar analysis might apply to other numerical schemes on curvilinear meshes. The flexibility on the direction of moving frames with spurious divergence removal, even beyond the tangent plane of the domain, can be adapted in many future numerical schemes for accuracy, stability, or many other applications.

References

- [1] P.-E. Bernard, J.-F. Remacle, R. Comblen, V. Legat, and K. Hillewaert, *High-order discontinuous Galerkin schemes on general 2D manifolds applied to shallow water equations*, J. Comput. Phys. **228** (2009), no. 17, 6514–6535.
- [2] Sehun Chun, *Method of moving frames to solve conservation laws on curved surfaces*, J. Sci. Comput. **53** (2012), no. 2, 268–294.
- [3] ______, Method of moving frames to solve the time-dependent Maxwell's equations on anisotropic curved surfaces: Applications to invisible cloak and ELF propagation, J. Compt. Phys. **340** (2017), 85–104.
- [4] ______, High-order covariant differentiation in application to helmholtz-hodge decomposition on curved surfaces, submitted (2020).

- [5] F. X. Giraldo and T. Warburton, A nodal triangle-based spectral element method for the shallow water equations on the sphere, J. Comput. Phys. **207** (2005), 129–150.
- [6] David A. Kopriva, Metric identities and the discontinuous spectral element method on curvilinear meshes, J. Sci. Compt. **26** (2006), no. 3, 301–327.
- [7] M. Läuter, F. X. Giraldo, D. Handorf, and K. Dethloff, A discontinuous Galerkin method for the shallow water equations in spherical triangular coordinates, J. Comput. Phys. 227 (2008), 10226–10242.
- [8] J. Marcon, M. Turner, D. Moxey, S.J. Sherwin, and J. Peiró, *A variational approach to high-order r-adaptation*, 26th International Meshing Roundtable, 2017.
- [9] J. Marcon, M. Turner, J. Peiró, D. Moxey, C. Pollard, H. Bucklow, and M. Gammon, *High-order curvilinear hybrid mesh generation for CFD simulations*, 2018 AIAA Aerospace Sciences Meeting (Reston, Virginia), no. January, American Institute of Aeronautics and Astronautics, jan 2018.
- [10] R. D. Nair, S. J. Thomas, and R. D. Loft, A discontinuous Galerkin global shallow water model, Mon. Wea. Rev. 133 (2005), 876–888.
- [11] Janusz A. Pudykiewicz, On numerical solution of the shallow water equations with chemical reactions on icosahedral geodesic grid, J. Comput. Phys. **230** (2011), 1956–1991.
- [12] J. F. Thompson, Z. U. Z. Warsi, and C. W. Mastin, Numerical grid generation, Elsevier Science Publishing, 1985.
- [13] M. Turner, D. Moxey, J. Peiró, M. Gammon, C. Pollard, and H. Bucklow, A framework for the generation of high-order curvilinear hybrid meshes for CFD simulations, Procedia Engineering 203 (2017), 206–218.
- [14] M. Turner, J. Peiró, and D. Moxey, *Curvilinear mesh generation using a variational framework*, Computer-Aided Design **103** (2018), 73–91.
- [15] Wikipedia contributors, *Earth radius Wikipedia, the free encyclopedia*, 2020, [Online; accessed 1-October-2020].
- [16] D. L. Williamson, J. B. Drake, J. J. Hack, R. Jakob, and P. N. Swarztrauber, A standard test set for numerical approximations to the shallow water equations in spherical geometry, J. Comput. Phys. 102 (1992), no. 1, 211– 224.